Impedance and Mössbauer spectroscopy study of BiCu$_3$Ti$_3$FeO$_{12}$ dielectric matrix

D. B. Freitas[1,2], M. H. Bezerra Júnior[1,2,5], R. G. M. Oliveira[2,*], J. E. V. de Morais[2],
V. L. Bessa[1,2], F. F. Carmo[2,6], M. S. Pereira[3], I. F. Vasconcelos[3], M. A. S. Silva[2],
H. D. de Andrade[4], I. S. Queiroz Júnior[4], R. S. Silva[7], and A. S. B. Sombra[2,4]

[1] *Telecommunication Engineering Department, Federal University of Ceará (UFC), P.O. Box 6007, Fortaleza, CE 60755-640, Brazil; https://www.locem.ufc.br*

[2] *Telecommunication and Materials Science and Engineering of Laboratory (LOCEM), Physics Department, Federal University of Ceará (UFC), Campus PICI, P.O. Box 6030, Fortaleza, CE, Brazil; https://www.locem.ufc.br*

[3] *Department of Metallurgical and Materials Engineering, Federal University of Ceará, Fortaleza, Brazil*

[4] *Federal University of Semiarid Region, UFERSA, Mossoró, RN 59625-900, Brazil*

[5] *Federal Institute of Ceará, Campus Fortaleza/IFCE, Fortaleza, CE 63400-000, Brazil*

[6] *Department of Organic and Inorganic Chemistry, Federal University of Ceará (UFC), Fortaleza, CE, Brazil*

[7] *Group Functional Nanomaterials, Physics Department, Federal University of Sergipe, Sao Cristóvão, SE 49100-000*

URL: https://www.locem.ufc.br, Brazil

ABSTRACT

In the present work, an electroceramic of the perovskite family, BiCu$_3$Ti$_3$FeO$_{12}$ (BCTFO), was synthesized by the solid-state reaction method. The structural study was performed by X-ray diffraction and Mössbauer and Raman spectroscopy. Electric and dielectric properties were analyzed by impedance spectroscopy and the Hakki-Coleman method. Due to the BCTFO is isostructural of the CaCu$_3$Ti$_4$O$_{12}$ (CCTO), the BCTFO presents as a promissory electroceramic. Mössbauer spectroscopy reveals paramagnetic spectra to BCTFO, with two octahedral sites for iron ions. Regarding dielectric properties, for 1 Hz, BCTFO presents a high relative dielectric permittivity ($\varepsilon_r \approx 1 \times 10^4$) and dielectric loss (tan $\delta > 1$) and $\varepsilon_r = 230.88$, tan $\delta \approx 1 \times 10^{-2}$ in the microwave range. The produced ceramic exhibited a high resonance frequency temperature coefficient (τ_f) with a value of + 2852 ppm °C^{-1}, making it a candidate for fabrication of the thermostable electroceramic composites with other ceramic matrices with negative τ_f values improving the thermal stability.

Address correspondence to E-mail: ronaldomaia@fisica.ufc.br; https://www.locem.ufc.br

Springer

1 Introduction

Rapid technological developments in recent decades have directed research seeking new materials to meet the growing needs by stable, miniaturized, and efficient devices. The need for miniaturization and improved efficiency in several devices, such as circuit components that operate in the microwave range, microelectronics, devices memory, optics, sound systems, satellites, and antennas, requires a search for dielectric materials with high relative permittivity and low dielectric losses [1–3]. For example, for radio frequency (RF) circuit applications, one desirable characteristic is a high dielectric constant, making $CaCu_3Ti_4O_{12}$ (CCTO) a promising material, though it does have a high dielectric loss value [4–6].

CCTO is a space-centered cubic body structure (Im-3 space group) and belongs to the perovskite family with the structural formula $ACu_3B_4O_{12}$ [7–9]. The "A" site can be occupied by large ions, such as Ca^{2+}, Sr^{2+}, and Bi^{3+}; trivalent rare earths; or ions that support high coordination numbers. "B" sites are generally occupied by Ti^{4+}, Mn^{4+}, Fe^{3+}, or Sn^{4+} or a combination of ions with adequate sizes for the octahedral site [8–14]. In the literature, an isostructural ceramic of CCTO is $BiCu_3Ti_3FeO_{12}$ (BCTFO), which presents a high relative dielectric permittivity, in the order of 1×10^4 and tan $\delta \approx 1$ at room temperature and at 100 Hz [11]. However, the BCTFO synthesis presented in this work is not completely pure, including a spurious phase of $FeBi_5Ti_3O_{15}$.

Figure 1 is shown the structure of the CCTO is, as an example of the $ACu_3B_4O_{12}$ system, It is represented by dodecahedral (Ca^{2+}) and octahedral (Ti^{4+}) symmetry ions. Cu^{2+} ions are in the planar square symmetry, inserted between dodecahedral and octahedral sites.
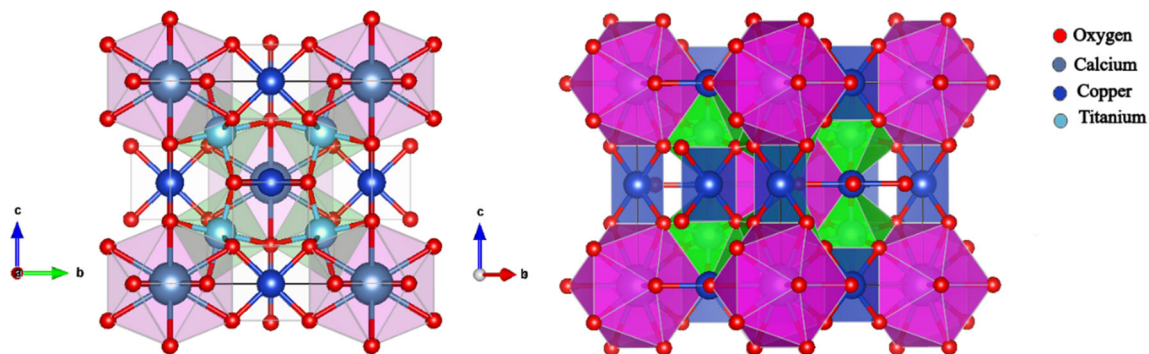
In this work, the BCTFO ceramic matrix was produced by the solid-state reaction method, and the structural evolution of the phase was analyzed by X-ray diffraction (XRD), Mössbauer spectroscopy, and Raman spectroscopy. Dielectric properties in the RF range were obtained by complex impedance spectroscopy (CIS) with temperature variation. For microwave range, the dielectric properties were analyzed by the Hakki-Coleman [15] and Silva-Fernandes-Sombra (SFS) methods [16]. The dielectric properties analyzed were relative permittivity (ε_r), dielectric loss (tan δ), and the resonant frequency temperature coefficient (τ_f).

2 Materials and methods

Polycrystalline samples of BCTFO were synthesized by a solid-state reaction method, according to the proposed stoichiometric reaction (Eq. 1). High-purity of Bi_2O_3 (Aldrich 99.9%), CuO (VETEC 99%), TiO_2 (Aldrich 99.8%), and Fe_2O_3 (Aldrich 99%) were mixed in a planetary ball mill (Pulverisette 5) for 6 h with zirconia balls (14 mm^3) in polyacetal jar (249 cm^3), in the proportion of 100 g of spheres to 10 g of powder, at 360 rpm. Subsequently, the oxide mixture was calcined at 800 °C for 4 h in air atmosphere.

$$\frac{1}{2}Bi_2O_3 + 3CuO + 3TiO_2 + \frac{1}{2}Fe_2O_3$$
$$\rightarrow BiCu_3Ti_3FeO_{12} \qquad (1)$$
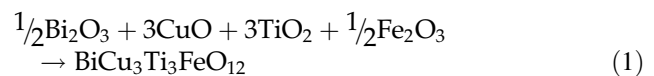
XRD patterns of powders were collected at room temperature in a X-Pert PRO MPD Panalytical diffractometer, operating with a Kα-Co source (λ = 1.789 Å) at 40 kV and 40 mA. Data were collected in a 2θ range of 20°–80°, step $\Delta\theta$ = 0.013, and 1°/min. The patterns were refined by the Rietveld

Fig. 1 Crystalline structure of CCTO (ICSD: 259850)

method [17, 18] using the General Structure Analysis System (GSAS) software [19].

Mössbauer spectra were acquired in transmission mode using a 57 Co(Rh) radioactive source mounted on a velocity driver, operating in sinusoidal mode. Data were evaluated by a least-square fitting to a series of discrete Lorentzian-shaped subspectra by the software package Normos. Isomer shifts (δ) are quoted with respect to α-Fe.

Raman spectra were measured at room temperature using a single grating spectrometer Jobin Yvon T64000, equipped with a N_2-cooled charge-coupled device (CCD) detection system. As the excitation source, a 532 nm beam from a Verdilaser (Coherent), with a power of 100 mW, was focused through a $50 \times$ microscope. The spectrometer slits were set for a 2 cm^{-1} resolution.

For electric measurements, the BCTFO powder was uniaxially pressed into a metallic molder at 17 mm diameter under 98 MPa and with two different heights. Both samples were sintered in air at 900 °C for 4 h. For electrical measurements, it was utilized a computer-controlled impedance analyzer (Solartron 1260), where was applied 1 Vac in the sample during the measurement, in the frequency range from 1 Hz to 1 MHz, in the temperature range between 200 and 460 °C. For dielectric measurements at the microwave range, Agilent N5230A and N5230C equipment were used to obtain the resonance frequency temperature coefficient (τ_f) and dielectric data, respectively. The pycnometry method was used to measure experimental densities of the ceramics.

3 Results and discussion

3.1 XRD

The BCTFO pattern is not indexed in ICSD database, thus, the phase confirmation was performed by matching with $NdCu_3Ti_3FeO_{12}$ (NCTFO; ICSD: 200954), which is an isostructural compound of BCTFO with a body-centered cubic perovskite-related structure of space group Im-3 (see the bars in Fig. 2). From the experimental diffractogram (Fig. 2), it can be seen that all peaks matched with the NCTFO pattern. The absence of secondary phases is attributed to the efficiency of the solid-state reaction method.
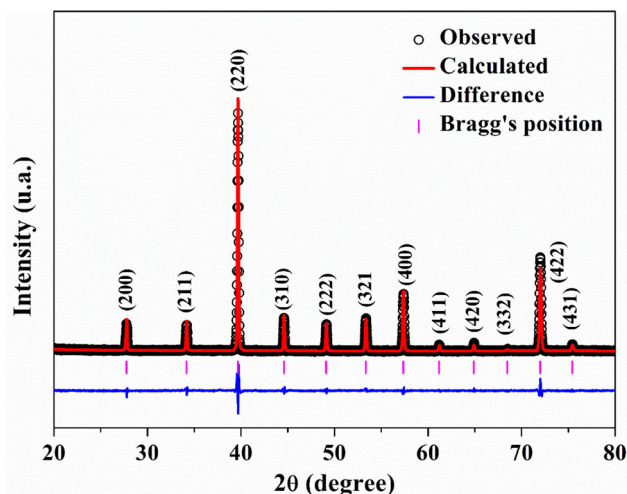

Fig. 2 XRD pattern of the BCTFO sample. Dots and solid lines describe the experimental data and best fit, respectively. Bars represent the ICSD-200954 standard pattern

Table 1 Lattice and agreement parameters obtained by Rietveld refinement

	BCTFO	NCFTO ICSD: 200,954
R_{wp}	16.38	–
χ^2	1.19	–
R_{Bragg}	3.54	–
a	7.45543 ± 0.00009	7.436
b	7.45543 ± 0.00009	7.436
c	7.45543 ± 0.00009	7.436
α	90.00	90.00
β	90.00	90.00
γ	90.00	90.00
V (Å^3)	414.40 ± 0.014	411.17
Space group	Im-3	Im-3

Rietveld refinement was performed by GSAS, with agreement and lattice parameters shown in Tables 1 and 2, demonstrating the phase formation of BCTFO from the reaction proposed in Eq. 1. The R_{Bragg}, R_{wp}, and χ^2 obtained in refinement demonstrated good agreement with experimental and calculated diffractograms and in accordance with the literature [20]. In refinement, the symmetry was the same of NCTFO, i.e., Im-3. BCTFO lattice parameters a, b, and c (7.455 Å) presented higher values than NCTFO (7.436 Å). This increase in lattice parameters and cell volume, compared with NCTFO (Table 1), is due the

Table 2 Atomic positions obtained by Rietveld refinement

| Atom	Ion	Site	BCTFO				NCFTO			
			x	y	Z	f	X	y	z	f
Nd	Nd^{3+}	2^a	–	–	–	–	0.0000	0.0000	0.0000	1.0000
Bi	Bi^{3+}	2^a	0.0000	0.0000	0.0000	1.000	–	–	–	–
Cu	Cu^{2+}	6b	0.0000	0.5000	0.5000	1.000	0.0000	0.5000	0.5000	1.0000
Ti	Ti^{4+}	8c	0.2500	0.2500	0.2500	0.750	0.2500	0.2500	0.2500	0.7500
Fe	Fe^{3+}	8c	0.2500	0.2500	0.2500	0.250	0.2500	0.2500	0.2500	0.2500
O	O^{2-}	24 g	0.29920	0.18201	0.0000	1.000	0.3017	0.1778	0.0000	1.000
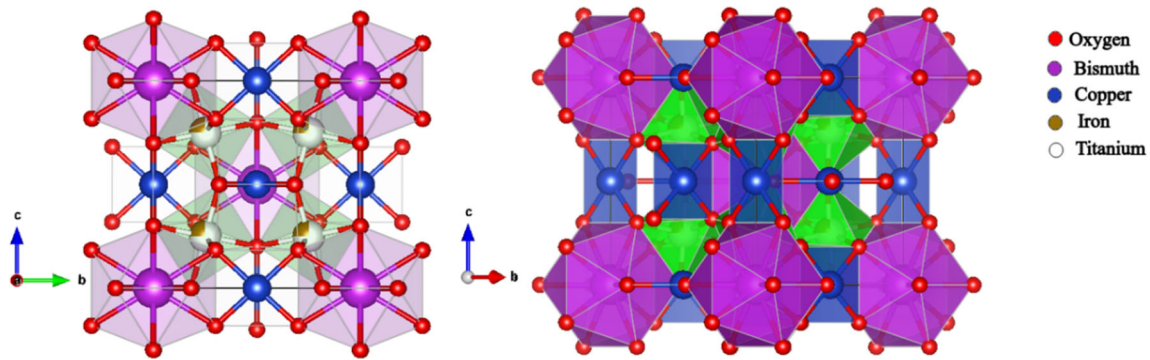
Fig. 3 BCTFO structure

higher ionic radius of Bi^{3+}(ionic radio (ir) = 1.17 Å) compared with Nd^{3+} (ir = 1.10 Å), both with coordination numbers = 8. Further, all diffraction peaks shifted for the lowest 2θ values, due to the substitution of neodymium by bismuth, following Bragg's Law. In the atomic position parameter, only the oxygen atom presented some change (Table 2), which can be explained by substitution of Nd^{3+} with Bi^{3+}. The crystalline structure of BCTFO, obtained by Rietveld refinement (Fig. 3), is very similar to CCTO (Fig. 1).

Relative density has a great impact on dielectric properties of electroceramics. The sintered ceramic presented a relative density 98.0%, where the relative density was calculated from monocrystal density calculated in the Rietveld refinement. This relative density shows a greater densification than the 96.0% found in the literature [11]. The parameters obtained by Rietveld refinement are shown in Table 1.

3.2 Mössbauer spectroscopy

The electronic and magnetic configuration of the iron atom in the BCTFO crystalline lattice was analyzed by Mössbauer spectroscopy at room temperature (Fig. 4). The spectrum showed a singlet, characteristic
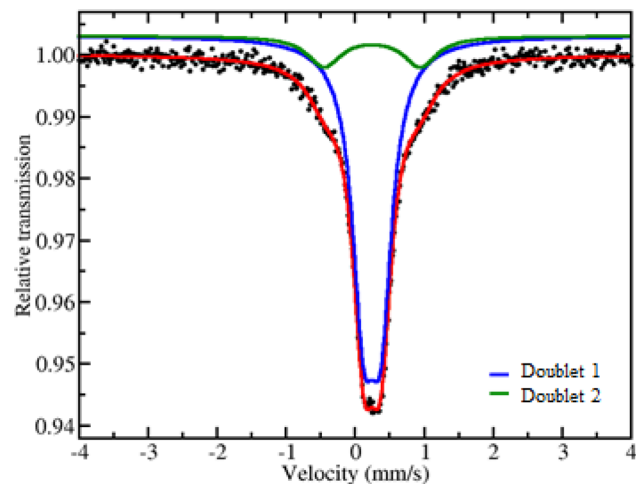
Fig. 4 Mössbauer spectrum of BCTFO. The dot points are experimental data and lines are: red (fitted spectrum), blue and green are the paramagnetic components of Mössbauer spectrum (Color figure online)

of paramagnetic materials without any magnetic characteristic nor any characteristic of the reagent (Fe_2O_3) utilized in the BCTFO synthesis, consistent with XRD results, however, the material exhibits magnetic behavior from − 268 to − 223 °C [21]. The analysis of hyperfine parameters, obtained from best

Table 3 Hyperfine parameters obtained from fitting the Mössbauer spectrum of BCTFO

Sites	δ (mm s^{-1})	Δ (mm s^{-1})	Γ (mm s^{-1})	Area (%)
Doublet 1	0.364	0.25	0.39	84.3
Doublet 2	0.365	1.39	0.59	15.7

fits to the data, are listed in Table 3. The spectrum was fitted by the superposition of two doublets with different quadrupole splitting values.

Based on the fitting, both doublets presented isomer shifts (δ) closer each other, frequently associated with Fe^{+3} in an octahedral symmetry and with covalent characteristics. This result confirms that the iron is in same symmetry of titanium (octahedral site in the CCTO structure). Moreover, iron ion distributions in the crystalline lattice indicate two different sites, as demonstrate by the fact that quadrupole splitting values (Δ) for doublets 1 and 2 are quite different: 0.25 and 1.39 mm/s, respectively. Results show two different iron sites, where Fe^{3+} in site 1 (84.3%) are octahedral with a symmetric neighborhood ($\Delta = 0.25$ mm s^{-1}), while Fe^{3+} in site 2 (15.7%) are octahedral with an asymmetric neighborhood. Notably, the linewidth (Γ) of doublet 2 is broadened in relation to site 1 because Fe in site 1, compared to site 2, presents a higher degree of local disorder.

3.3 Raman spectroscopy

Vibrational properties were investigated through Raman spectroscopy. Raman spectra of the BCTFO sample were recorded in the spectral region between 200 and 1000 cm^{-1}, using a 532 nm laser line as the excitation source. From XRD results, BCTFO exhibited a body-centered cubic primitive (Im-3) group, containing 20 atoms per unity. Group theory predicts that Raman active modes for the Im-3 group are distributed among the irreducible representation as [22]:

$$\Gamma_{Raman} = 2A_g + 2E_g + 4F_g \qquad (2)$$

The room temperature Raman spectrum for BCTFO (Fig. 5) shows five of the eight predicted symmetry modes.

Based on literature about the CCTO structure [5, 22–24], the symmetry modes are identified as $F_g(1) = 270$ cm^{-1}, $A_g(1) = 457$ cm^{-1}, $A_g(2) = 500$ cm^{-1}, $F_g(3) = 556$ cm^{-1}, and $F_g(4) = 695$ cm^{-1}.
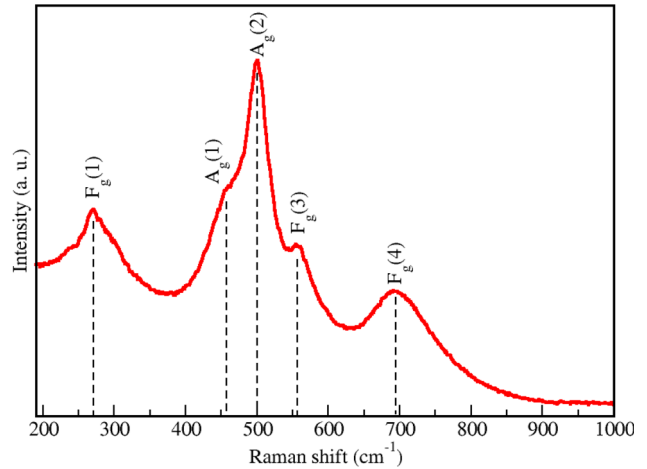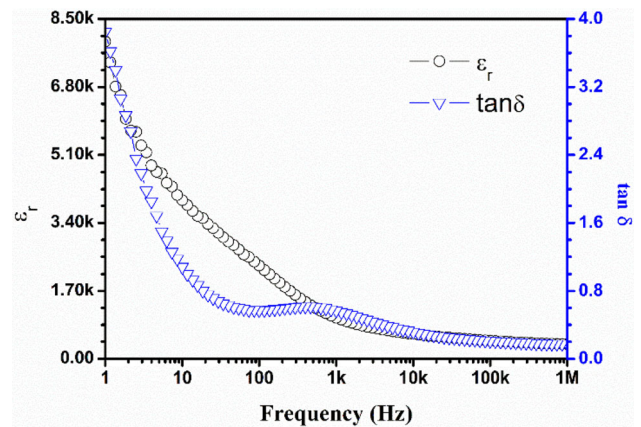

Fig. 5 Raman spectrum of BCTFO

Fig. 6 Dielectric spectra for BTCFO at room temperature

In the region of the Raman spectrum around of the 500 cm^{-1} there is an overlap of the $A_g(1)$, $A_g(2)$, and $F_g(3)$ modes. Following lattice dynamics calculations, the 270, 457, and 500 cm^{-1} transitions are TiO$_6$ rotation-like modes. The peak around 556 cm^{-1} is assigned to the Ti–O–Ti anti-stretching mode of the TiO$_6$ octahedra. The $F_g(4)$ mode has been predicted to appear around 708 cm^{-1}, and the mode near 695 cm^{-1} has been attributed to the symmetric stretching breathing of the TiO$_6$ octahedra. Based on the group analysis by Kolev et al. [22], only Ti vibrations are active in Raman spectra.

3.4 Electric and dielectric characterization

To analyse electrical properties (dielectric constant, losses, activation energy, electric modulus, and conductivity), the CIS measurements were done [25] from 1 Hz to 1 MHz and at different temperatures
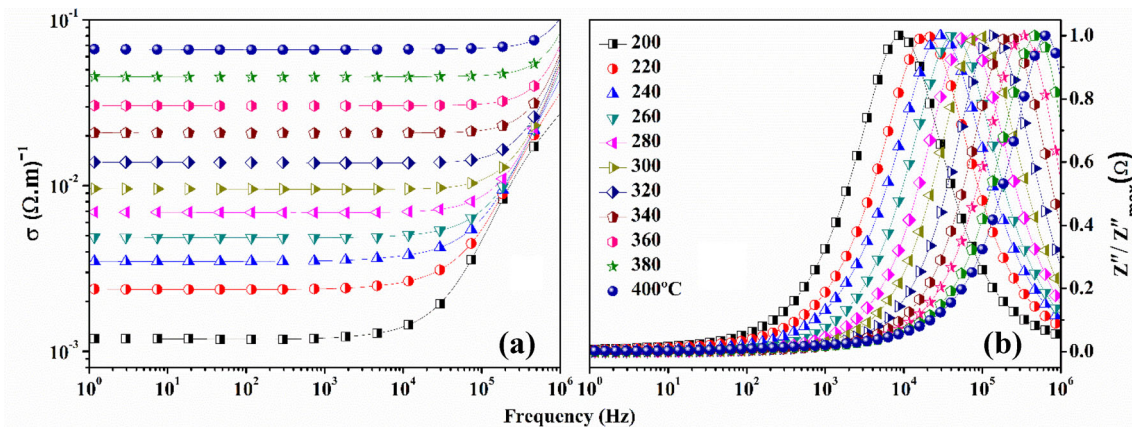
Fig. 7 **a** Conductivity and **b** normalized impedance versus frequency at temperatures ranging from 200 to 400 °C, as indicated in the legend
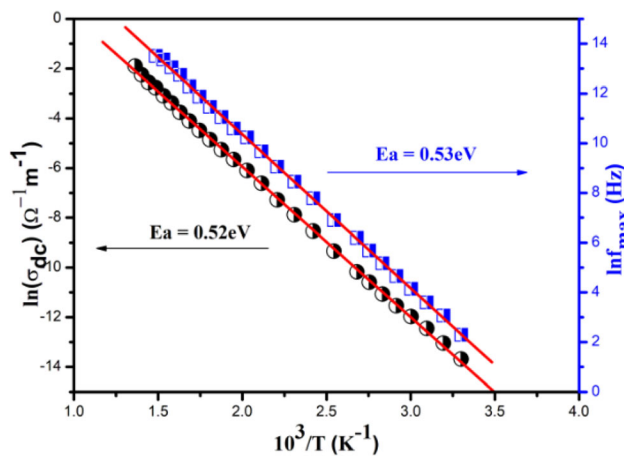

Fig. 8 Arrhenius plots showing the dependence of σ_{dc} and $f_{\max}$ (peak) versus 1000/T

(30–460 °C). These dielectric properties are often represented in terms of complex dielectric permittivity (ε^*), electric modulus (M^*), and complex impedance (Z^*).

At room temperature, dielectric measurements for BCFTO present high relative dielectric permittivity (giant permittivity; $\varepsilon_r \approx 10^3$) and dielectric loss (tan $\delta \approx 4$) at low frequency, as shown in Fig. 6. There is a good similarity of this dielectric properties presented by BCTFO with CCTO ceramic, i.e., BCFTO appears as candidate for colossal permittivity ceramic.

Figure 7a and b show the conductivity and normalized impedance spectra at different temperatures, respectively. In Fig. 7a, an increase in conductivity with variation of temperature and frequency was observed. In Fig. 7b, it was observed a displacement of the relaxation peaks with the temperature increase.

These behaviors indicate that BFCTO exhibits some thermally activated conduction process. Thermo-activated processes can obey the Arrhenius relation (Eqs. 3 and 4), and the activation energy can be determined.

$$\ln(f) = \ln(f_0) - \left(\frac{E_a}{k}\right) * \left(\frac{1}{T}\right) \tag{3}$$

$$\ln(\sigma) = \ln(\sigma_0) - \left(\frac{E_a}{k}\right) * \left(\frac{1}{T}\right) \tag{4}$$

where E_a is the activation energy related to the thermo-activated process, which is in general, a conduction process. k is the Boltzmann constant (in eV), and T is absolute temperature. σ and f are the DC conductivity and frequency of the maxima present in the imaginary impedance spectrum, respectively, while σ_0 and f_0 are pre-exponential factors.

Figure 8 presents the Arrhenius curve, according to Eqs. 3 and 4, for dc conductivity and relaxation frequency for BCTO sample. Note that both curves are for thermo-activated process and presents values of activation energy (E_a) close to each other. Indicating that the thermo-activated process observed in Fig. 7a is same observed in 7b.

The temperature coefficient of capacitance (TCC) depicts how capacitance varies in a given temperature range. This parameter is an important factor for the development of devices that operate in the RF region [26]. For one ideal capacitor, the TCC values can be closer to zero. Which means that the capacitors must present electric stability under external effects, such as temperature variation. [27]. In this work, the TCC was measured from 30 to 100 °C. Table 4 shows the TCC values for BCTFO at various frequencies. BCTFO shows high positive TCCs (above 100 kHz)

Table 4 TCC values for BCTFO

Frequency (Hz)	TCC (ppm °C^{-1})
1 k	− 2435.34
10 k	1431.79
100 k	16,528.12
1 M	19,583.28

and, thus, is a promising candidate for thermostable ceramics when mixed with other oxides, whose TCC has opposite signs.

The electrical responses of electroceramics arise from the sum of electrical responses of the morphology of the ceramic as grain, grain boundary, and electrode interface. Each electric response is associated with a half-circle for each contribution in the Nyquist plot. Some cases, two or more half-circles can overlap with each other showing only one or two half-circle. One way to observe electrical contributions of the grain and grain boundary from the Nyquist diagrams is the equivalent circuit simulation, in which one associated resistor–capacitor (RC) can represent the electric response of each ceramic region. Figure 9 presents the Nyquist plots for some measurements and the fitted by equivalent circuits. At high-frequency region, the grain effects are very evident while at low frequency (grain boundary response) the presence of a second semicircle is not evidenced. From the simulation of the equivalent circuit (inset in Fig. 9b), the effect of grain and grain boundary can be separated. All fitting presented errors varying from 0.2 to 3.7%. Two types of relaxation behaviours are observed in low and high-frequency regions at low temperatures [28]. However, these two relaxations are well-defined, as shown in Table 5, showing the grain resistivity decreasing with temperature, with the grain boundary exhibiting charge carrier diffusion due to the coarse electrode surfaces [29].

Fig. 9 Nyquist plots at **a** 30, **b** 100, **c** 200, and **d** 300 °C with an electrical equivalent circuit
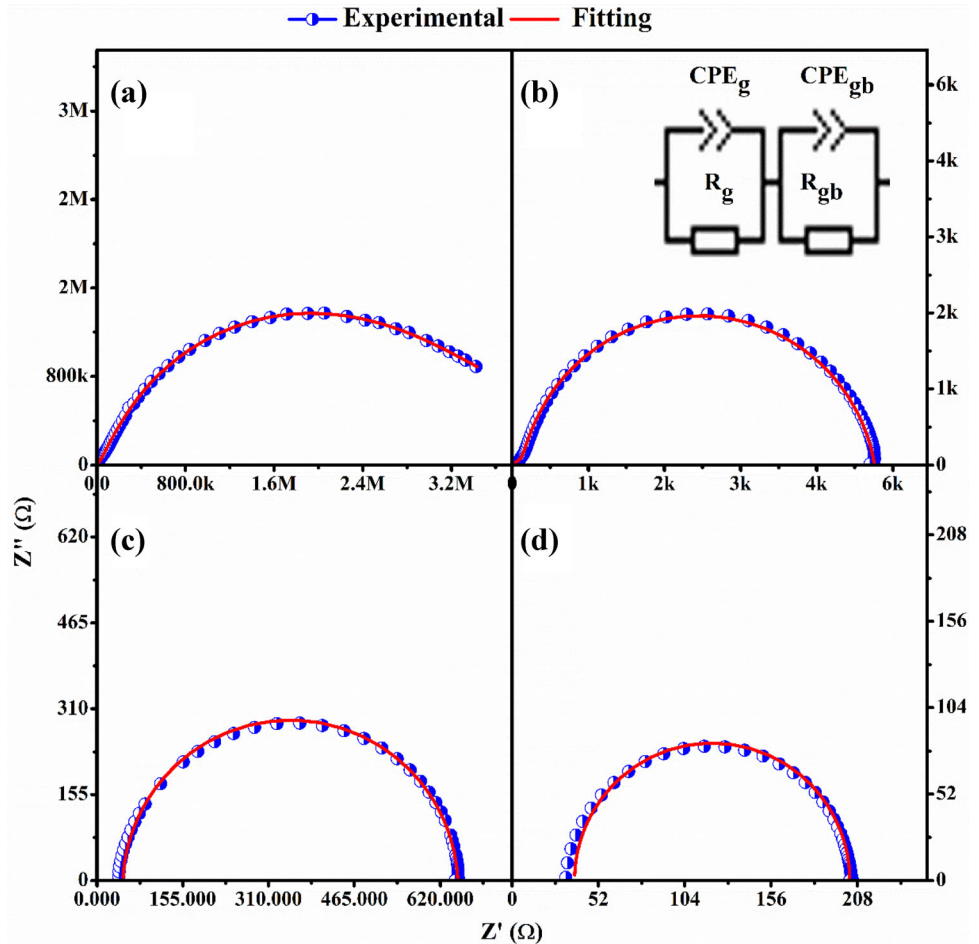
Table 5 Fitting equivalent circuit parameters for BCTFO

Temperature (°C)	Grain			Grain boundary		
	R_1 (Ω)	P_1 (F)	N_1	R_2 (Ω)	P_2 (F)	N_2
30	2.72×10^6	1.45×10^{-8}	0.851	2.23×10^6	2.47×10^{-7}	0.498
100	1.34×10^5	1.29×10^{-8}	0.857	5.05×10^4	5.02×10^{-7}	0.782
200	4.88×10^3	1.17×10^{-8}	0.750	1.25×10^4	2.30×10^{-7}	0.599
300	6.05×10^2	4.89×10^{-8}	0.598	4.70×10^2	4.87×10^{-7}	0.488

R resistance, *P* equivalent to capacitance (Faraday), *N* deviation of ideal capacitance

The dielectric response in the microwave range were measured with Hakki-Coleman and SFS methods. For both methods, one ceramic cylinder was fabricated with 14.80 mm diameter and 8.94 mm height. BCTFO presented high relative dielectric permittivity at 1.7 GHz ($\varepsilon_r = 230.88$) with tan $\delta = 2.08 \times 10^{-2}$. The temperature coefficient of the resonant frequency (τ_f), measured in the microwave range, was 2852 ppm $°C^{-1}$. These results suggest its potential use for miniaturization of devices operating in this range, and BCTFO also presented higher relative dielectric permittivity compared to other ceramics [4]. For τ_f, although the higher positive value indicates BCTFO is thermally unstable, it makes BCTFO a good candidate for formulating new, thermally stable composites with other ceramic oxides, such as $NdAlO_3$, $LaAlO_3$, $PbZrO_3$–CeO_2 [4] and $Na_2Nb_4O_{11}$ [30], in processes based on Silva et al. [31].

4 Conclusion

BCTFO ceramic was successfully produced by a low-cost, solid-state reaction route, without the presence of spurious phases. XRD results indicated a single perovskite-related structure phase, which was confirmed by Raman analyses. Mössbauer results suggested that iron atoms are in the Fe^{3+} state and surrounded by two different chemical environments characterized by two singlets, both with octahedral symmetry and without magnetic character. The dielectric properties (ε_r and tan δ) presented by BCTFO in the RF and microwave ranges demonstrated high values compared with other ceramics, and τ_f presented a higher positive value (2852 ppm $°C^{-1}$), which allows BCTFO to be combined with other ceramic oxides to found thermally stable ceramic composites.

References

1. A.J. Moulson, J.M. Herbert, *Electroceramics: Materials, Properties, Applications* (Wiley, Oxford, 2003).

2. A. Petosa, *Dielectric Resonator Antenna Handbook* (Artech House, Boston, MA, 2007).

3. D. Kajfez, P. Guillon, *Dielectric Resonators*, 2nd edn. (Tucker, Lisle, 1998).

4. M.T. Sebastian, *Dielectric Materials for Wireless Communication* (Elsevier, Amsterdam, 2008). https://doi.org/10.1016/B978-0-08-045330-9.X0001-5

5. A.F.L. Almeida, P.B.A. Fechine, M.P.F. Graça, M.A. Valente, A.S.B. Sombra, Structural and electrical study of CaCu3-Ti4O12 (CCTO) obtained in a new ceramic procedure. J. Mater. Sci. Mater. Electron. **20**, 163–170 (2009). https://doi.org/10.1007/s10854-008-9675-4

6. S. De Almeida-Didry, C. Autret, A. Lucas, C. Honstettre, F. Pacreau, F. Gervais, Leading role of grain boundaries in colossal permittivity of doped and undoped CCTO. J. Eur. Ceram. Soc. **34**, 3649–3654 (2014). https://doi.org/10.1016/j.jeurceramsoc.2014.06.009

7. J. Li, M.A. Subramanian, H.D. Rosenfeld, C.Y. Jones, B.H. Toby, A.W. Sleight, Clues to the giant dielectric constant of CaCu 3 Ti 4 O 12 in the defect structure of "SrCu 3 Ti 4 O 12." Chem. Mater. **16**, 5223–5225 (2004). https://doi.org/10.1021/cm048345u

8. M.A. Subramanian, A.W. Sleight, $ACu_3Ti_4O_{12}$ and $ACu_3Ru_4O_{12}$ perovskites: high dielectric constants and valence degeneracy. Solid State Sci. **4**, 347–351 (2002). https://doi.org/10.1016/S1293-2558(01)01262-6

9. M.A. Subramanian, D. Li, N. Duan, B.A. Reisner, A.W. Sleight, High dielectric constant in $ACu_3Ti_4O_{12}$ and $ACu_3Ti_3FeO_{12}$ phases. J. Solid State Chem. **151**, 323–325 (2000). https://doi.org/10.1006/jssc.2000.8703

10. P. Shi, P. Liang, Z. Yang, J. Yi, C. Ma, X. Chao, Z. Yang, Intrinsic and extrinsic dielectric responses in $BiCu_3Ti_3FeO_{12}$ ceramics. Ceram. Int. **41**, 3672–3676 (2015). https://doi.org/10.1016/j.ceramint.2014.11.037

11. P. Liang, X. Wang, X. Chao, Z. Yang, Electric response and improved dielectric properties in $BiCu_3Ti_3FeO_{12}$. J. Alloys Compd. **734**, 9–15 (2018). https://doi.org/10.1016/j.jallcom.2017.11.049

12. C.-M. Wang, K.-S. Kao, S.-Y. Lin, Y.-C. Chen, S.-C. Weng, Processing and properties of $CaCu_3Ti_4O_{12}$ ceramics. J. Phys. Chem. Solids. **69**, 608–610 (2008). https://doi.org/10.1016/j.jpcs.2007.07.049

13. M. Ahmadipour, M.F. Ain, Z.A. Ahmad, A short review on copper calcium titanate (CCTO) electroceramic: synthesis, dielectric properties, film deposition, and sensing application. Nano-Micro Lett. **8**, 291–311 (2016). https://doi.org/10.1007/s40820-016-0089-1

14. R.N.P. Choudhary, U. Bhunia, Structural, dielectric and electrical properties of $ACu_3Ti_4O_{12}$ (A = Ca, Sr and Ba). J. Mater. Sci. **37**, 5177–5182 (2002). https://doi.org/10.1023/A:1021019412533

15. B.W. Hakki, P.D. Coleman, A dielectric resonator method of measuring inductive capacities in the millimeter range. IEEE Trans. Microw. Theory Tech. **8**, 402–410 (1960). https://doi.org/10.1109/TMTT.1960.1124749

16. M.A.S. Silva, T.S.M. Fernandes, A.S.B. Sombra, An alternative method for the measurement of the microwave temperature coefficient of resonant frequency (τf). J. Appl. Phys. **112**, 074106 (2012). https://doi.org/10.1063/1.4755799

17. H.M. Rietveld, Line profiles of neutron powder-diffraction peaks for structure refinement. Acta Crystallogr. **22**, 151–152 (1967). https://doi.org/10.1107/S0365110X67000234

18. H.M. Rietveld, A profile refinement method for nuclear and magnetic structures. J. Appl. Crystallogr. **2**, 65–71 (1969). https://doi.org/10.1107/S0021889869006558

19. B.H. Toby, EXPGUI, a graphical user interface for GSAS. J. Appl. Crystallogr. **34**, 210–213 (2001). https://doi.org/10.1107/S0021889801002242

20. C. Pascoal, R. Machado, V.C. Pandolfelli, Determinação de fase vítrea em bauxitas refratárias. Cerâmica **48**, 61–69 (2002). https://doi.org/10.1590/S0366-69132002000200004

21. A. Haque, A. Shukla, U. Dutta, D. Ghosh, A. Gayen, P. Mahata, M. Vasundhara, A.K. Kundu, M.M. Seikh, Incompatible magnetic and dielectric properties of $BiCu_3-xMn_xTi_4-yM_yO_{12}$ (x = 0 & 0.5; y = 1 & 1.5 and M = Fe & Mn).

22. N. Kolev, R.P. Bontchev, A.J. Jacobson, V.N. Popov, V.G. Hadjiev, A.P. Litvinchuk, M.N. Iliev, Raman spectroscopy of $CaCu_3Ti_4O_{12}$. Phys. Rev. B **66**, 132102 (2002). https://doi.org/10.1103/PhysRevB.66.132102

23. K. Chen, Y. Wu, J. Liao, J. Liao, J. Zhu, Raman and dielectric spectra of $CaCu_3Ti_{3.9}O_{12}$ Ceramics. Integr. Ferroelectr. **97**, 143–150 (2008). https://doi.org/10.1080/10584580802089023

24. C. Mu, Y. Song, H. Wang, X. Wang, Room temperature magnetic and dielectric properties of cobalt doped $CaCu_3Ti_4O_{12}$ ceramics. J. Appl. Phys. **117**, 17B723 (2015). https://doi.org/10.1063/1.4916116

25. J.R. MacDonald, Impedance spectroscopy: emphasizing solid materials and systems. Appl. Opt. **28**, 1083 (1989)

26. B. Lee, I. Abothu, P. Raj, C. Yoon, R. Tummala, Tailoring of temperature coefficient of capacitance (TCC) in nanocomposite capacitors. Scr. Mater. **54**, 1231–1234 (2006). https://doi.org/10.1016/j.scriptamat.2005.12.026

27. R.G.M. Oliveira, D.B. Freitas, G.S. Batista, J.E.V. de Morais, V.C. Martins, M.M. Costa, M.A.S. Silva, D.X. Gouvêa, C. Singh, A.S.B. Sombra, Dielectrical and structural studies of composite matrix $BiVO_4$–$CaTiO_3$ and temperature effects by impedance spectroscopy. J. Mater. Sci. Mater. Electron. **29**, 16248–16258 (2018). https://doi.org/10.1007/s10854-018-9714-8

28. K. Hirota, G. Komatsu, M. Yamashita, H. Takemura, O. Yamaguchi, Formation, characterization and sintering of alkoxy-derived bismuth vanadate. Mater. Res. Bull. **27**, 823–830 (1992). https://doi.org/10.1016/0025-5408(92)90177-2

29. Y. Zhang, T. Tong, W. Kinsman, P. Jiang, G. Yin, S. Li, Dielectric and impedance analysis of La doped-$TbMnO_3$. J. Alloys Compd. **549**, 358–361 (2013). https://doi.org/10.1016/j.jallcom.2012.09.005

30. R.G.M. Oliveira, D.B. Freitas, M.C. Romeu, M.A.S. Silva, A.J.M. Sales, A.C. Ferreira, J.M.S. Filho, A.S.B. Sombra, Design and simulation of $Na_2Nb_4O_{11}$ dielectric resonator antenna added with Bi_2O_3 for microwave applications. Microw. Opt. Technol. Lett. **58**, 1211–1217 (2016). https://doi.org/10.1002/mop.29765

31. M.A.S. Silva, R.G.M. Oliveira, A.S.B. Sombra, Dielectric and microwave properties of common sintering aids for the manufacture of thermally stable ceramics. Ceram. Int. (2019). https://doi.org/10.1016/j.ceramint.2019.07.021

Ceram. Int. **46**, 5907–5912 (2020). https://doi.org/10.1016/j.ceramint.2019.11.043

Springer